



# A robust active power control algorithm to maximize wind farm power tracking margins in waked conditions

Simone Tamaro, Filippo Campagnolo, and Carlo L. Bottasso

Wind Energy Institute, Technical University of Munich, 85748 Garching b. München, Germany

**Abstract.** We present an active wind farm power control (APC) algorithm that operates wind turbines to maximize their power availability and robustly track a reference power signal in the presence of turbulent wind lulls. The operational setpoints of the wind turbines are optimized with an augmented version of FLORIS that combines induction control with wake steering to deflect low-momentum wakes and increase power margins. The algorithm also features a proportional-integral closed loop  
5 inspired by the literature to correct potential errors deriving from the offline calculation of the setpoints.

First, we demonstrate the methodology in steady-state conditions, showing how the availability of power is increased by mitigating wake interactions. We observe that the methodology is particularly effective in conditions of strong wake impingement, occurring in scenarios of high power demand. Next, considering two wind farm layouts, we compare the performance of the algorithm to three state-of-the-art reference APC formulations in unsteady scenarios using large-eddy simulations coupled  
10 with the actuator line method (LES-ALM). We show that the occurrence and treatment of local, temporary instances of power unavailability ( *saturations* ) dramatically affects power tracking accuracy. The proposed method yields superior power tracking due to the increased power margins that limit the occurrence of saturation events. Additionally, we show that this performance is achieved with reduced structural fatigue.

## 1 Introduction

15 As renewable energy sources occupy a larger portion of the electricity mix, they must also become capable of providing extra functionalities to the grid, beyond the pure generation of power (Aho et al., 2012; Ela et al., 2014). Among these extra operating modes, active power control (APC) is a strategy where generating assets are intentionally operated below their maximum output to satisfy operational constraints imposed by the transmission system operator (TSO).

In the context of wind energy, the APC problem is particularly challenging due to the dynamics of mesoscale weather  
20 phenomena, the two-way interaction of the atmospheric boundary layer with a wind farm, the complex development of the flow within the plant, and its local interaction with the aeroelastic behavior of wind turbines. The maximum available power that can be generated by a wind farm at any given time is strongly influenced by site and local turbine-specific ambient conditions, which change over time in uncertain and difficult-to-predict ways (van Kuik et al., 2016). As a result, sudden drops in wind speed or inaccuracies in forecasts can result in inadequate power reserves, making it difficult to follow a given reference  
25 signal (Fleming et al., 2016).



In a wind farm, the situation is further complicated by the presence of low-momentum turbulent wakes, which lead to power losses and contribute to fatigue loading on frequently waked turbines (Vermeer et al., 2003; Lee et al., 2013; Guilloré et al., 2024). A variety of approaches has been suggested to reduce the impact of wake effects, such as induction, yaw control, and mixing (Meyers et al., 2022). Yaw control, in particular, involves “steering” the wakes away from downstream turbines. Its effectiveness in boosting power has been demonstrated in numerical simulations (Jiménez et al., 2010; Fleming et al., 2014; Vollmer et al., 2016), wind tunnel experiments (Medici and Alfredsson, 2006; Campagnolo et al., 2016; Schottler et al., 2017), and real-world field trials (Fleming et al., 2019; Doekemeijer et al., 2021).

Different APC approaches have been described and tested in the literature.

The most straightforward method uses an open-loop strategy, where each turbine is given a predefined power-share setpoint (Fleming et al., 2016). However, unsurprisingly, the absence of feedback reduces the power tracking accuracy, particularly under strong wake impingement conditions. Additionally, uniformly distributing power among turbines may result in suboptimal performance, as the local power availability varies among different turbines due to wake effects.

Various authors have used model predictive control (MPC) for APC (Shapiro et al., 2017; Boersma et al., 2018). The main drawback of such methods lies in the need for a dynamic farm flow model, which increases complexity and computational cost. While such methods undoubtedly have their own merits, here we are interested in solutions that are closer to practical applicability and a more rapid uptake from industry.

Classical PID (proportional-integral-derivative) controllers are widely used in an extremely broad range of different industrial applications. As such, they have also been widely studied for wind farm APC (van Wingerden et al., 2017). While these methods lack the sophistication of MPC, they do not require a wind farm flow model and can offer quick response times with straightforward implementations.

The APC PI (proportional-integral) controller proposed by van Wingerden et al. (2017) operates on the tracking error, adjusting the power demands to match a reference, and distributes power among the turbines in a predefined static manner. The approach incorporates gain scheduling, which is based on the proportion of wind turbines in saturation, defined as those whose available power is less than the demanded power.

Multiple authors have formulated APC methods that – beyond tracking a power signal – also try to control dynamic loads in order to reduce fatigue (Kanev et al., 2018; Vali et al., 2019; Silva et al., 2022). In particular, Vali et al. (2019) introduced a nested PI loop to dynamically adjust the setpoints of the wind turbines, with the goal of equalizing their loading. So far, these PI-based methods have been applied only to induction control.

Although these methods perform well in many conditions, their performance may be significantly impacted by saturation events, caused by a temporary local lack of power (*reserves*). Saturations harm tracking accuracy, and therefore their occurrence should be limited as much as possible. Saturations, or more in general power margins, are not explicitly accounted for nor monitored in the existing APC PI implementations, which is a gap in the existing literature.

The effects of wind variability can be mitigated by hybridizing wind farms with storage solutions (Sinner et al., 2023). While storage has a crucial role to play in the transition towards a large penetration of renewables, here we are interested in mitigating



60 the effects of wind variability on APC performance without the addition of extra hardware, but simply through a better, more robust way of controlling wind farms.

The success of wake steering in power boosting control makes this technology a primary candidate to increase power reserves, thereby improving APC tracking robustness. In fact, some initial attempts in this direction have been recently presented by Starke et al. (2023); Oudich et al. (2023). These studies showed that the time scales required by wake redirection are compatible with secondary grid frequency regulation. However, these same studies lack a comprehensive modeling of misaligned conditions, which are significantly affected by curtailed operation (Cossu, 2021; Campagnolo et al., 2023; Heck et al., 2023).

This paper introduces a novel wind farm control algorithm designed to enhance power tracking accuracy under conditions of strong, persistent wakes, especially when the power demand approaches the maximum available power of the wind farm. The algorithm improves tracking performance by explicitly maximizing power reserves to mitigate the impact of wind lulls. This innovative approach integrates wake steering with induction control. The associated power losses in misaligned conditions are accounted for with a recent model by Tamaro et al. (2024a). Wake steering is achieved using an open-loop, model-based optimal setpoint scheduler. This approach is based on the offline optimization of the control setpoints that, once stored in look-up tables, are interpolated at runtime. The resulting relatively simple online implementation, which is still based on a sophisticated offline optimization, has recently gained popularity in power-boosting wind farm control (Meyers et al., 2022), and it is being deployed in a growing number of industrial applications. Induction control is implemented through a rapid closed-loop corrector to enhance tracking accuracy (Tamaro and Bottasso, 2023).

The methodology described in this paper has been preliminarily tested in a simulation environment by Tamaro and Bottasso (2023), and also demonstrated through experiments performed with scaled models in a boundary layer wind tunnel by Tamaro et al. (2024b). However, an exhaustive description of the formulation and an extensive validation were still missing. Compared to these preliminary works, here we more thoroughly describe and improve our APC method, expand its testing across a wider range of operating conditions through new dedicated simulations, and we analyze the results also in terms of saturation events and fatigue loading. The new methodology is demonstrated on a small cluster of wind turbines with different layouts, first in steady-state with the FLOW Redirection and Induction in Steady-state (FLORIS v3) code (Gebraad et al., 2016; National Renewable Energy Laboratory, 2023), and then in unsteady conditions using a TUM-modified version of NREL's large-eddy simulation with actuator line model (LES-ALM) Simulator fOr Wind Farm Applications (SOWFA) (Fleming et al., 2014; Wang et al., 2019).

The paper is organized as follows: Sect. 2 presents the new formulation, the tools developed to support it, and the reference APC algorithms. Section 3 describes the simulation set-up and reports and discusses results from the steady and unsteady analyses. Finally, Sect. 4 concludes and offers an outlook towards future work.



90 **2 Active power control formulation**

**2.1 Robust APC: closed loop with maximum reserve (CL + MR)**

The central component of the wind farm control system is an open-loop, model-based optimal setpoint scheduler. This scheduler determines the yaw misalignment of each turbine and calculates its contribution (i.e., power share) to meet the power demand set by the TSO, based on the current ambient conditions. Real-time wind speed and turbulence intensity can be obtained from SCADA data. Wind sensing techniques (Bertelè et al., 2021, 2024) can be employed to account for wind shear, for a finer adjustment of the controller to the ambient conditions. Additionally, a feedback loop is used to correct any tracking errors that may occur from the open loop in real-time. A block diagram of the control system is provided in Fig. 1.

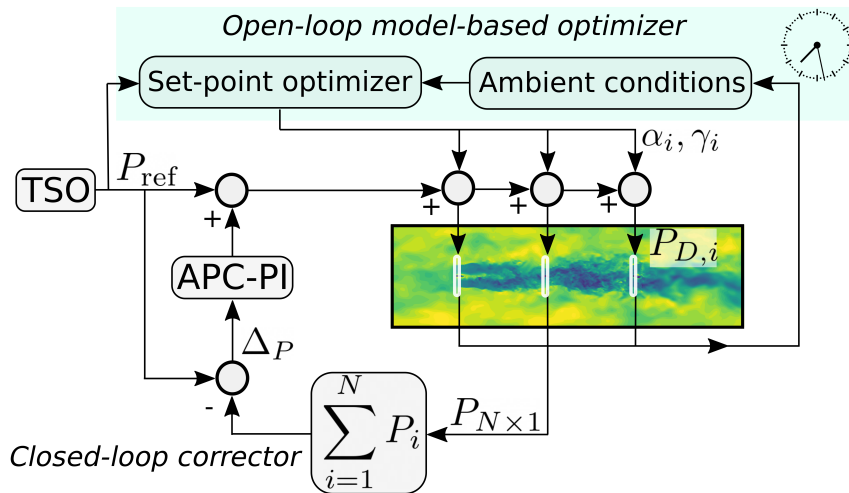


**Figure 1.** Schematic representation of the APC controller, featuring an open-loop model-based optimizer and a closed-loop corrector.

The closed and open loops operate at different time rates due to the varying time scales of the physical phenomena they control. Specifically, the open loop, which adjusts the yaw setpoints  $\gamma_i$  and power shares  $\alpha_i$ , updates at a slow rate, because of the time required by wakes to propagate downstream. On the other hand, the closed loop operates at a much faster rate, as it is charged with locally correcting small tracking errors. In this study, the open loop is updated three orders of magnitude faster than the closed loop.

**2.1.1 Open-loop setpoint optimal scheduler**

The open-loop part of the algorithm calculates the optimal setpoints for yaw misalignment and power share. These are determined through a gradient-based optimization process that maximizes the minimum power reserve across the farm while meeting a specified overall power demand.



The power of the  $i$ -th turbine is noted  $P_i = P_i(\mathbf{A}_i, \mathbf{u}_i)$ , where  $\mathbf{A}_i$  indicates the local ambient conditions, here assumed to include wind speed  $U_\infty$ , wind direction  $\psi$ , vertical shear  $k$ , and turbulence intensity TI. The symbol  $\mathbf{u}_i$  indicates the control inputs, namely power share  $\alpha_i = P_i / \sum_{i=1}^N P_i$  and yaw misalignment  $\gamma_i$ . Power is computed using a wind farm flow model based here on FLORIS. The power of misaligned and curtailed wind turbines is computed based on Tamaro et al. (2024a).

The maximum power that turbine  $i$  can capture by modifying its control setpoints  $\mathbf{u}_i$  (with the setpoints of the other turbines held constant) is calculated as

$$P_{a,i} = \arg \max_{\mathbf{u}_i} P_i(\mathbf{A}_i, \mathbf{u}_i) = \frac{1}{2} \rho \pi R^2 U^3 C_P \eta_P(\gamma_i, \delta_i),$$

where  $\rho$  is the air density,  $C_P$  is the power coefficient,  $R$  is the rotor radius,  $U$  is the local rotor-equivalent wind speed. The symbol  $\eta_P$  indicates the power scaling factor used by Tamaro et al. (2024a) to model power losses due to yaw  $\gamma$  and tilt  $\delta$ . The algorithm seeks the setpoint combination that maximizes the minimum power ratio  $P_i/P_{a,i}$  across all  $N$  turbines in the farm, while ensuring the power demand of the TSO, noted  $P_{\text{ref}}$ , is met. This can be expressed as

$$\min_{\mathbf{u}} \max_{i \in [1, N]} \frac{P_i}{P_{a,i}} \text{ such that } \sum_{i=1}^N P_i = P_{\text{ref}}. \quad (1)$$

In fact, a smaller power ratio  $P_i/P_{a,i}$  results in a larger reserve  $m_i = 1 - P_i/P_{a,i}$ , which can be used to mitigate drops in wind. Equation (1) represents a constrained optimization problem. However, this optimization does not need to be carried out in real-time during operation. Instead, it is performed offline for a range of ambient conditions and wind farm curtailment levels. The results are stored in a look-up table, which is then interpolated at runtime, similarly to the approach used in power-boosting wind farm control (Meyers et al., 2022). When the maximum reserve of the farm is zero, the optimization provides the traditional maximum power solution (Meyers et al., 2022), making power boosting a limiting case of the proposed APC formulation. This feature ensures a seamless and smooth transition between the power-boosting and APC modes of operation.

By using a load surrogate model (Guilloré et al., 2024), damage could be readily introduced as a cost term or a constraint in the optimization, although this option was not considered further in this work.

### 2.1.2 Closed-loop corrector

The closed-loop corrector is directly adopted from the work of van Wingerden et al. (2017). It features a simple PI feedback loop that operates based on the power tracking error, which results from the open-loop part of the control system. The tracking error  $\Delta_P$  is defined in this work as

$$\Delta_P = P_{\text{ref}} - \sum_{i=1}^N P_i. \quad (2)$$

The PI gains are obtained with a tuning procedure based on a simple Simulink (The MathWorks Inc., 2022) model described in Sect. 2.6. van Wingerden et al. (2017) proposed a gain scheduling based on the number of saturated turbines. This approach is not used here because it was found that – when used with a limited number of wind turbines – it may cause abrupt variations



in the gains that can lead to instabilities. Instead, when a turbine saturates, its local power tracking error is redistributed equally among the non-saturated ones, as proposed by Vali et al. (2019). This is explained in more detail later in Sect. 2.3.

The controller features an anti-windup term on the integrator when all turbines are saturated, and the integrator is reset when no saturation occurs, as proposed by Silva et al. (2022).

## 140 2.2 Reference APC formulations for performance comparison

Three reference wind farm APCs are considered with the goal of comparing the performance of the proposed power reserve boosting method, namely:

- **Open loop (OL)**: this simple approach assigns predetermined setpoints  $\alpha_i$  to each turbine as fractions of the power demanded by the TSO, so that  $\sum_{i=1}^N \alpha_i = 1$ . The setpoints  $\alpha_i$  are scheduled with the instantaneous wind direction to account for different local power availabilities. The  $\alpha_i$ 's are predicted with the FLORIS model described in Sect. 2.5.  
145
- **Closed loop (CL)**: this method is the same as OL with the addition of the PI feedback loop described in Sect. 2.1.2. For OL and CL, the power setpoints are determined from preliminary simulations in which the turbines operate in greedy mode under the same ambient conditions of the APC runs.
- **Closed loop with load balance (CL + LB)**: this method consists of CL without the fixed scheduling of the power share setpoints  $\alpha_i$ . Instead, an additional PI loop is nested to distribute the  $\alpha_i$ 's with the purpose of balancing loads within the wind farm (Vali et al., 2019). In this work, the tower base fore-aft bending moment is chosen as the target load. As proposed by Silva et al. (2022), the mean load is computed considering only non-saturated turbines, and an anti-windup term is added to the integrator of a turbine when it saturates.  
150

It is important to mention that CL, CL+LB and CL+MR feature the same PI control block described in Sect. 2.1.2, so the closed-loop part is exactly the same. A visual comparison of all APC strategies considered in this work is presented in Fig. 2.  
155

## 2.3 Identification and treatment of saturation conditions

Local turbine saturations are detected when the blade pitch lies at its optimal value, and the tracking error exceeds a given threshold, set to 1% of rated power. Both conditions need to be verified to activate saturation. The threshold for the pitch angle is set to  $0.4^\circ$ . When a wind turbine enters saturation, its power demand is fixed to the last value recorded, while its local tracking error is equally redistributed to non-saturated turbines in the form of additional power demand in order to ensure that  $\sum_{i=1}^N \alpha_i = 1$ . This way locally isolated saturation events – even if persistent – do not introduce significant tracking errors as long as other turbines with enough power reserve can compensate.  
160

On the other hand, conditions in which all wind turbines are close to saturation are particularly harmful to the tracking accuracy, as a cascade effect can be triggered that may lead to all turbines being saturated. In fact, in this case, all wind turbines operate in greedy mode and, if the TSO demand drops, a significant (negative with respect to Eq. 2) tracking error will arise.  
165

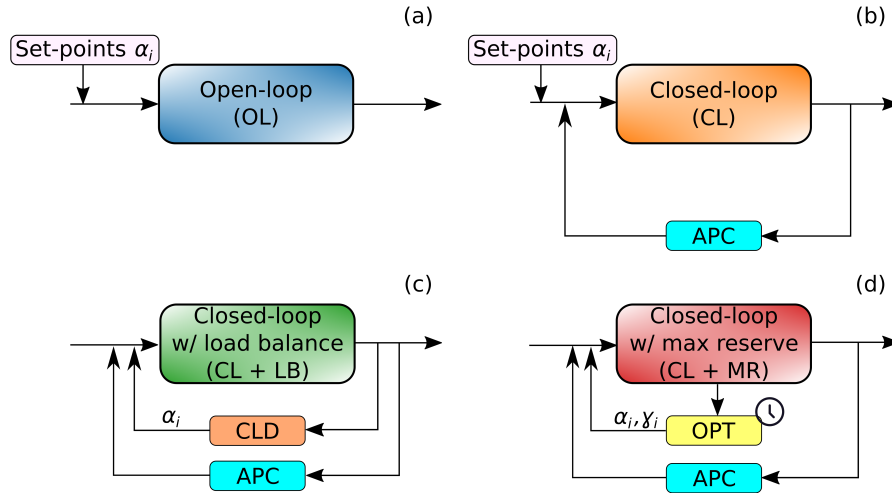


**Figure 2.** Visual comparison of the three APCs considered in this work, open loop (a), closed loop (b), closed loop with load balancing setpoint distributor (c), closed loop with max-reserve setpoint distributor (d).

To avoid this situation, when the wind farm produces more than the instantaneous demand (with a threshold set to 3% of the turbine rated power), every saturation condition is forcibly reset.

## 2.4 Wind turbine controller

The wind turbine controller is characterized by two distinct regimes, namely:

- 170 – Below rated: the blades lie at the optimal pitch angle, while the generator torque  $Q$  is related to the rotor speed  $\Omega$  as  $Q(\Omega) = \kappa\Omega^2$ , where  $\kappa$  is a constant (Bossanyi, 2000).
- Above rated: each turbine yields its demanded power by collectively pitching the blades based on a standard PI loop.  $Q$  and  $\Omega$  are fixed and equal to the rated values, i.e.  $Q_R$  and  $\Omega_R$  respectively.

The transition between the two regimes occurs when  $\Omega$  exceeds  $\Omega_R$ . Turbines can track a given power demand  $P_D$  by adjusting  
 175  $\Omega_R$  as

$$\Omega_R = \sqrt[3]{\frac{P_D}{\kappa}}, \quad (3)$$

and by setting  $Q_R = P_D/\Omega_R$ . In case a gearbox is present, the rotor angular velocity should be corrected by the gearbox ratio to yield the high-speed shaft velocity.

180 With this control approach, the blade pitch angle  $\theta$  can be used to measure the margin of a curtailed wind turbine (Tamaro and Bottasso, 2023). Generally, high values of  $\theta$  indicate a high margin since the turbine operates at a sub-optimal  $C_P$ . The lowest limit for  $\theta$  is the optimal pitch angle  $\theta_{opt}$ , which yields the maximum  $C_P$ .



This type of controller was chosen because it explicitly receives a power demand as an input, which is accurately tracked using the blade pitch angle. Other control methods could also be used, possibly significantly affecting the APC performance.

## 2.5 Steady-state model for control synthesis

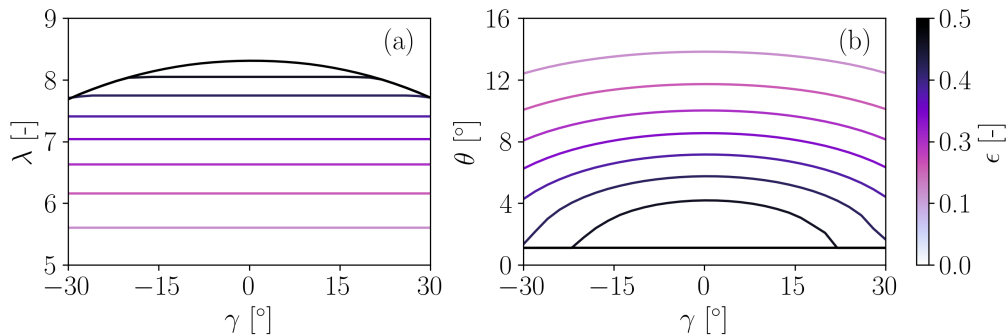
185 The engineering farm flow model FLORIS v3 (National Renewable Energy Laboratory, 2023) is used both to synthesize the open-loop part of the controller and to perform steady-state analyses. The Gauss Curl Hybrid wake model (King et al., 2021) is used, with default wake parameters. To model off-rated operation, the lookup tables of power coefficient  $C_P$  and thrust coefficient  $C_T$  are modified to consider curtailed conditions.

Since off-rated operation spans a wide range of  $C_T$  – and misaligned operation is strongly dependent on  $C_T$  (Cossu, 2021; 190 Heck et al., 2023) – the standard FLORIS model is coupled with an analytical model to predict rotor performance (Tamaro et al., 2024a), rather than relying on the  $\cos^{P_p}$  method (Liew et al., 2020). The model uses the operating pitch angle  $\theta$  and the tip speed ratio  $\lambda = \Omega R/U$  of the turbine to determine how much power is lost for a given misalignment angle  $\gamma$ . Since  $\theta$  and  $\lambda$  are the results of the control strategy, which is itself reacting to  $\gamma$ , the problem is implicit. To compute the entries of the lookup tables  $C_P = C_P(\lambda, \theta, \gamma)$  and  $C_T = C_T(\lambda, \theta, \gamma)$ , the balance equation between aerodynamic power  $P$  and demanded power  $P_D$  195 is solved iteratively. Following Tamaro et al. (2024a), the equation

$$P = \frac{1}{2} \rho \pi R^2 U^3 C_P(\lambda, \theta, \gamma) = Q(P_D, \Omega) \Omega = P_D \quad (4)$$

is solved for  $\lambda$  with  $\theta = \theta_{\text{opt}}$ . If the resultant  $\Omega$  is lower than the rated value  $\Omega_R$  – which is computed from  $P_D$  via Eq. (3) – the turbine operates in below-rated conditions, whereas if  $\Omega \geq \Omega_R$  it is in rated conditions. In this case, Eq. (4) is instead solved for  $\theta$ , with  $\lambda = \Omega_R R/U$ .

200 In the optimization phase, we normalize  $P_D$  using the rated power  $P_R$ , defining a curtailment parameter  $\epsilon = P_D/P_R$ . Figure 3 presents the setpoints of  $\lambda$  and  $\theta$  for a range of  $\epsilon$  values for  $U = 8 \text{ m s}^{-1}$ , plotted as functions of the misalignment  $\gamma$ .



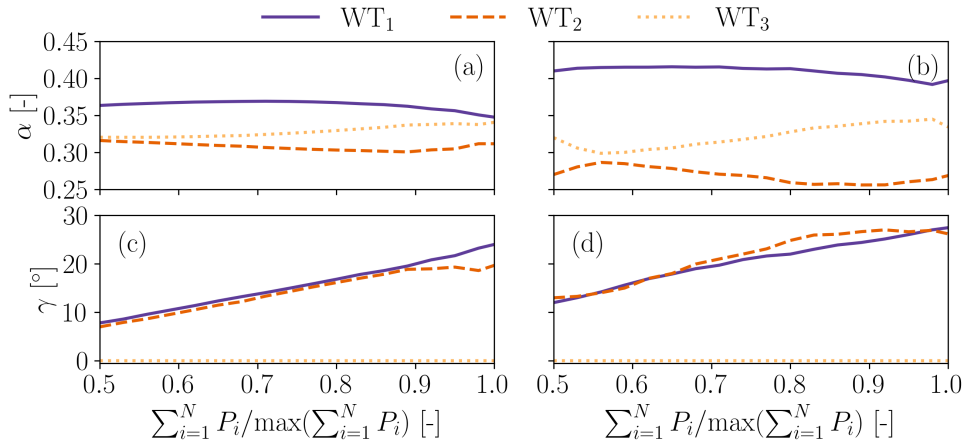
**Figure 3.** Control setpoints  $\lambda$  (a) and  $\theta$  (b) plotted as functions of the misalignment angle  $\gamma$  for different values of the normalized power demand  $\epsilon$  for  $U = 8 \text{ m s}^{-1}$ .

Figure 3a shows that when  $\epsilon$  is decreased,  $\lambda$  is reduced due to the smaller  $\Omega_R$  (see Eq. 3). Accordingly, the blade pitch angle in Fig. 3b increases to reduce the power output.

205 The quantities  $\epsilon$  and  $\gamma$  are used as optimization variables. The curtailment  $\epsilon$  is limited to  $0 \leq \epsilon_i \leq P_{a,i}/P_R$  to ensure that the optimizer never asks for a power demand that exceeds the locally available one, while the yaw angle is bounded to  $\gamma_{\min} \leq \gamma \leq \gamma_{\max}$ , these turbine-dependent limits typically being imposed by ultimate and/or fatigue loads.

A different optimization is solved for each ambient condition (wind speed, wind direction, optionally turbulence intensity), to generate the associated setpoints. When the optimization converges, the resulting power share setpoints are computed as  
 210  $\alpha_i = P_i / \sum_{i=1}^N P_i$ , and they are stored together with the yaw setpoints in a lookup table. The optimization problem is solved with the gradient-based Sequential Quadratic Programming (SQP) method (Brayton et al., 1979). During operation,  $\alpha_i$  and  $\gamma_i$  are linearly interpolated from the lookup tables based on the average power demand computed over the last 30 seconds. Clipping to the last available value of the lookup table is applied to avoid extrapolation.

Figure 4 reports the yaw setpoints and power share percentages that maximize the smallest power margin for the aligned  
 215 turbines of Sect. 3.1.



**Figure 4.** Optimal setpoints that maximize the minimum power margin for the three aligned turbines of Sect. 3.1. Power setpoints (a,b), yaw setpoints (c,d). Wind direction  $\psi = 7.1^\circ$  (a,c), wind direction  $\psi = 3.6^\circ$  (b,d). The power setpoints are plotted as fractions of the available wind farm power.

The figure shows that the most upstream turbines are misaligned with respect to the wind, with the goal of increasing the power reserves of the downstream ones. The wind turbines are misaligned more when the rotor overlap is larger. The power shares result from different local inflow conditions, yaw misalignment, and wake effects.

## 2.6 Digital twin for gain tuning

220 The gains of the APC controllers are synthesized with a reduced wind turbine model coupled with a simple dynamic wake model. The Simulink (The MathWorks Inc., 2022) implementation features three wind turbines with their own controllers. The



drivetrain dynamics of the turbines are modeled with transfer functions based on results from wind tunnel experiments (Campagnolo et al., 2022). The Jensen wake model (Jensen, 1983) is combined with the instantaneous thrust coefficient  $C_T$  to estimate the wake deficit for downstream wind turbines. Wake effects are delayed based on the local wind speed and wind turbine separation distance to simulate the time needed for wake effects to propagate downstream. Figure 5 presents a sketch of the digital twin.

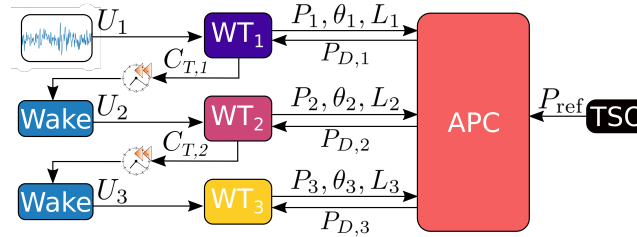


**Figure 5.** Block diagram of the structure of the Simulink model used for optimizing the APC gains.

The wind turbines are assumed to be fully aligned, and the inflow is taken from wind tunnel measurements in a turbulent boundary layer. The CL and CL + LB APC supercontrollers are implemented in the digital twin. Their gains are optimized with the interior-point gradient-based algorithm, where the cost function is the Root Mean Square (RMS) of the power tracking error.

To improve the robustness of the gains, zero-mean white noise with a variance of  $18 \text{ kW}^2$  is added to the input measured power.

In the case of CL+LB, the cost function is defined as  $J = 0.75\bar{\Delta}_P + 0.25\sum_{i=1}^N\bar{\Delta}_{L,i}$ , and it represents the weighted sum of the non-dimensional tracking error  $\bar{\Delta}_P$  and non-dimensional overall load-balancing error  $\bar{\Delta}_{L,i}$ . Both quantities are non-dimensionalized to lie in the interval  $[0,1]$ .

### 3 Results

#### 3.1 Numerical set-up

Tests are performed on an array of three wind turbines located at a streamwise distance of 4 diameters (4D). Two scenarios are considered, with wind directions  $\psi$  equal to  $3.6^\circ$  and  $7.1^\circ$ , corresponding to 75% and 50% rotor overlaps, respectively. These conditions involve partial wake impingement, which is particularly relevant for fatigue considerations. The most upstream turbine is labeled  $WT_1$ , the most downstream one  $WT_3$ , and the one in the center is referred to as  $WT_2$ . Simulations are conducted using the IEA 3.4 MW reference wind turbine, a typical onshore machine with a contemporary design (Bortolotti et al., 2019). Here, we only note that the turbine has a  $5^\circ$  up tilt angle, i.e.,  $\delta = -5^\circ$  (Tamaro et al., 2024a), the optimal pitch is  $\theta_{opt} = 1.09^\circ$ , and the constant  $\kappa$  for the generator torque in below-rated regime is  $\kappa = 1,804 \text{ kN m s}^2 \text{ rad}^{-2}$ . The maximum yaw rate is equal to  $0.8^\circ \text{ s}^{-1}$ . The PI gains for the CL+MR controller are  $K_{APC}^P = 1.3127 [-]$  and  $K_{APC}^I = 0.2063 \text{ s}^{-1}$ , while the



ones for the coordinated load distribution (CLD) of CL+LB are  $K_{CLD}^P = 0.03427 \text{ Nm}^{-1}$  and  $K_{CLD}^I = 0.07959 \text{ Nm}^{-1} \text{ s}^{-1}$ . The APC open loop is updated every 30 seconds, and the closed loop every 0.01 seconds. In CL+LB, loads are filtered by applying exponential smoothing with a time constant of 0.1 s.

LES-ALM simulations are used for testing the performance of the new APC formulation, because they can represent the complex dynamics typical of wind turbine wakes and their interactions (Wang et al., 2019). An in-house version of the LES-ALM code SOWFA is used (Troldborg et al., 2007; Wang, 2021), which includes the smearing correction to blade tip forces proposed by Meyer Forsting et al. (2019).

The use of a small cluster of turbines is motivated by the computational cost of the simulations. However, the small distance between the turbines implies a short propagation time that requires a very robust APC. Furthermore, this simple layout allows to clearly isolate and understand the effects that take place in the farm.

The LES Cartesian mesh comprises approximately 14.3 million cells and includes six refinement levels. The smallest cells measure 1 m and are located in correspondence of the three rotors. Two tilted hexahedral regions are used to refine the wind farm array. The computational domain, grids, and turbine layout are shown in Fig. 6.

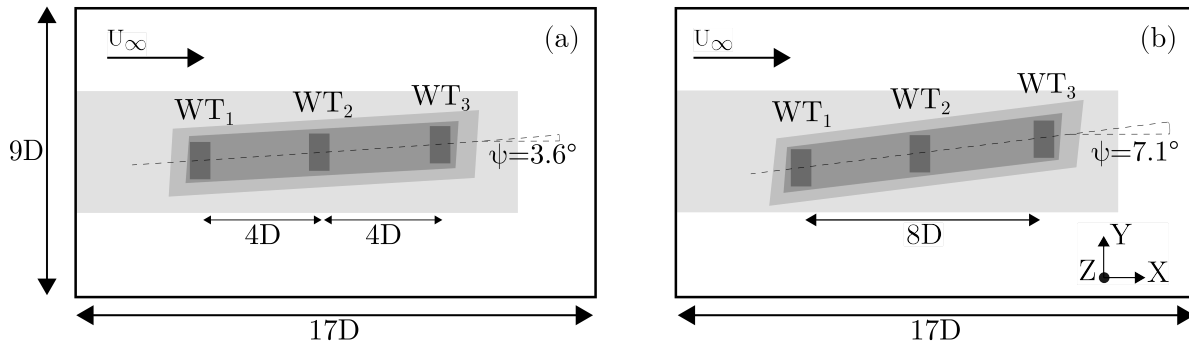


**Figure 6.** Wind farm layout and simulation scenarios for 75% (a), and 50% (b) rotor overlap. The shaded areas indicate the mesh refinement levels.

Unsteady tests are run with a turbulent wind obtained from a precursor generated in stable atmospheric conditions with periodic inlet-outlet boundary conditions. The inflow is characterized by a turbulence intensity  $TI = 5.7\%$ , a hub height wind speed  $U_\infty = 9.54 \text{ ms}^{-1}$ , a power-law shear coefficient  $k = 0.21$ , and an integral length scale of turbulence at hub height equal to  $0.79D$ . The normalized mean streamwise velocity and turbulence intensity fields at the inlet –  $4D$  upstream of  $WT_1$  – are included in Fig. 7.

Each simulation is run for 1,200 seconds. The first 200 seconds are considered as the initial transient, and hence they are discarded. The total time of 1,000 seconds is approximately equivalent to 1.6 standard 10-minute seeds, which is less than the minimum recommended value (Liew and Larsen, 2022), but in line with the numerical study of van Wingerden et al. (2017). Given the short duration, results are likely dependent on the specific inflow realization, especially at high power demands due

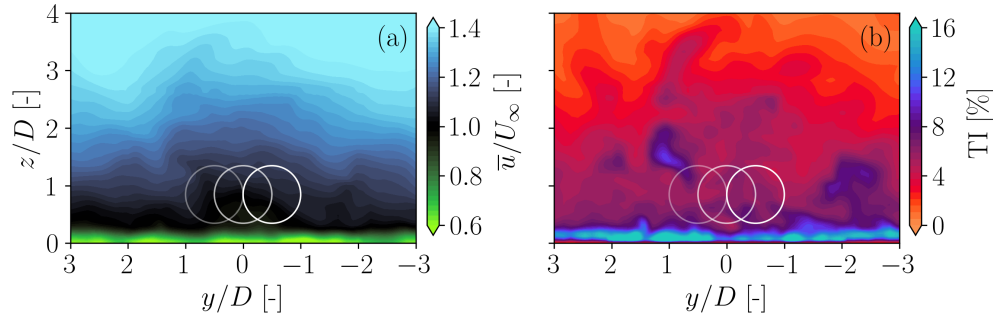


**Figure 7.** Slices of inflow fields. Time-averaged wind speed normalized by the free-stream wind speed (a); turbulence intensity field (b). The locations of the three wind turbines for  $\psi = 7.1^\circ$  are marked with a line transparency that increases along with the distance from the inflow slice.

to the multiple simultaneous saturations. To mitigate this effect, simulations are also performed with all turbines operating in greedy mode. The results of the different APC formulations are then compared to the corresponding greedy results.

### 270 3.2 Reference power demand signal

A dynamic reference power signal typical of automatic generation control (AGC) is used as a reference power signal. AGC is the secondary response regime of grid frequency control, and it consists of the modification of the power output of a plant depending on dynamically changing requests by the TSO (Aho et al., 2012). A similar signal has also been considered by other authors (Fleming et al., 2016; van Wingerden et al., 2017; Shapiro et al., 2017; Boersma et al., 2018; Vali et al., 2019). The  
 275 signal is defined as

$$P_{\text{ref}}(t) = P_{\text{greedy}}(\Psi) \left( b + c n_k^{\text{AGC}}(t) \right), \quad (5)$$

where  $n_k^{\text{AGC}}(t)$  is a normalized perturbation from a standard test signal,  $P_{\text{greedy}}$  is the time-averaged available power of the wind farm in greedy conditions, and  $b$  and  $c$  are parameters that shift and change the amplitude of  $n_k^{\text{AGC}}$ , respectively. Figure 8 shows the time history of the normalized perturbation  $n_k^{\text{AGC}}$ .

280  $P_{\text{greedy}}$  is computed on a preliminary simulation under the same ambient conditions of the APC runs, where the turbines operate aligned and in greedy mode. The value  $c = 0.1$  is used in all cases, while three different values of  $b$  are considered, i.e.  $b = [0.7, 0.8, 0.9]$ . For  $\psi = 7.1^\circ$ , an additional run at  $b = 0.85$  is also performed. In general, a higher value of  $b$  makes the TSO signal harder to track, due to a closer proximity to the greedy power available.

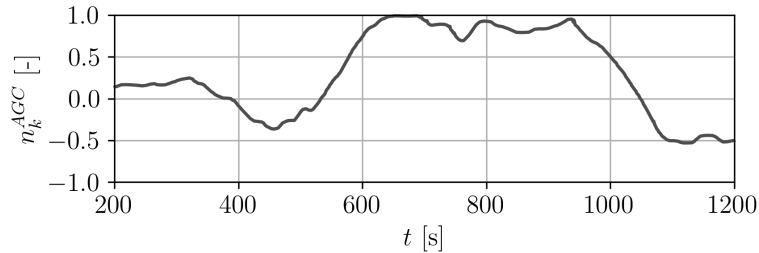


**Figure 8.** Time history of the normalized perturbation signal  $n_k^{AGC}$  of Eq. (5).

### 3.3 Steady-state analysis

285 First, the method CL+MR is compared to OL using FLORIS. This analysis is performed on the cluster of three turbines at a streamwise distance of 4D and three inflow angles  $\psi = [0^\circ, 3.6^\circ, 7.1^\circ]$ , corresponding to rotor overlaps of 100%, 75%, and 50%, respectively. Results are shown in Fig. 9.

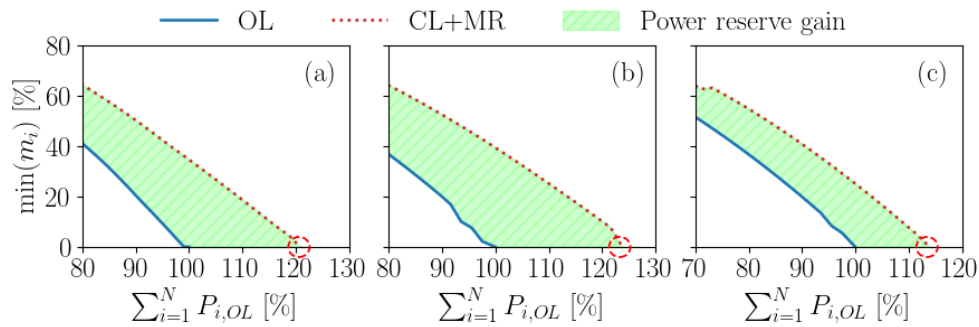


**Figure 9.** Smallest local power reserve in percentage obtained with a purely inductive wind farm control (labeled OL), and with a controller that dispatches power and yaw set-points to optimize power reserves (labeled CL+MR).  $\psi = 0^\circ$ , i.e. 100% rotor overlap (a);  $\psi = 3.6^\circ$ , i.e. 75% rotor overlap (b);  $\psi = 7.1^\circ$ , i.e. 50% rotor overlap (c). On the  $x$ -axis, wind farm power is normalized by the maximum value for OL. The red circle indicates the classical maximum power solution.

290 The figure shows that the margin drops to zero in correspondence with the maximum power of the plant, whereas it increases as the power demand is lowered and the wind turbines are curtailed. Wake steering effectively extends the power available to the wind farm. In agreement with the literature, the effectiveness of wake steering is dependent on  $\psi$ . In all cases, the proposed CL+MR strategy can increase the power margin for all wind farm power demands. The highest power gain is observed for  $\psi = 3.6^\circ$ , in exceedance of +20%. As the power demand  $\sum_{i=1}^N P_{i,OL}$  is reduced, the added margin of CL+MR diminishes



since wake effects get weaker – both in terms of velocity deficit and also in terms of deflection – because of the lower  $C_T$ . For the three wake overlaps, the classical maximum power solutions are shown in the figure using red circle symbols.

### 295 3.4 Unsteady conditions

Next, results from the LES-ALM simulations are presented. Figure 10 reports slices of the time-averaged free-stream velocity fields  $\bar{u}(x, y)$  at hub height, normalized by the free-stream value  $U_\infty$ . Figure 11 shows the turbulence intensity TI. The plots are shown for OL and the proposed CL+MR for  $\psi = 3.6^\circ$  and  $\psi = 7.1^\circ$ , at  $b = 0.8$ . CL and CL+LB are not shown for the sake of simplicity, since they are qualitatively similar to OL.

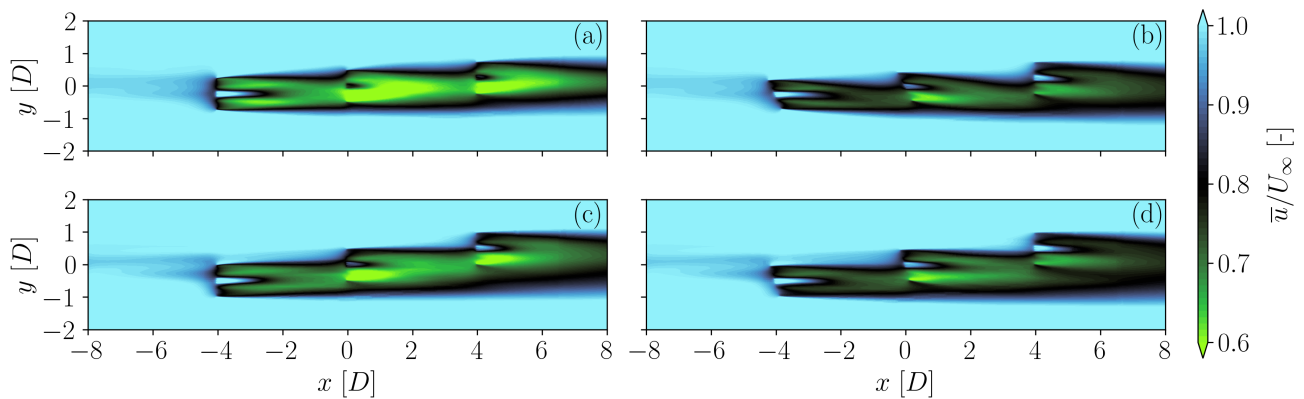


**Figure 10.** Time-averaged streamwise velocity fields for a TSO power request of  $b = 0.8$ , for two APC control strategies: open loop (OL) (a,c), closed loop with optimal power reserve (CL+MR) (b,d).  $\psi = 3.6^\circ$  (a,b),  $\psi = 7.1^\circ$  (c,d). The slices are extracted at hub height.

300 These plots highlight the different extent of wake impingement that occurs on the downstream rotors at  $\psi = 3.6^\circ$  and  $\psi = 7.1^\circ$ . Similarly, Figs. 10b and 10d allow one to appreciate the effect of yaw misalignment on the wakes, which are significantly deflected to one side compared to fully aligned conditions. The effect is remarkable when considering that the turbines are curtailed, and hence the smaller  $C_T$  reduces the deflection compared to a greedy scenario.

The plots of turbulence intensity in Fig. 11 highlight the fact that waked rotors operate in regions of significant turbulence, 305 as expected.

Next, the time series of produced and demanded power are shown in Figs. 12 and 13 for  $\psi = 3.6^\circ$  and  $\psi = 7.1^\circ$ , respectively. The wind farm power from a preliminary simulation where the turbines operate aligned in greedy mode is shown in the background in grey. This greedy power can differ and even be lower than the one produced in the APC cases, because of the slightly different wake effects due to curtailment. Nevertheless, it is reported here to provide a proxy for the instantaneous 310 power available in the wind farm.

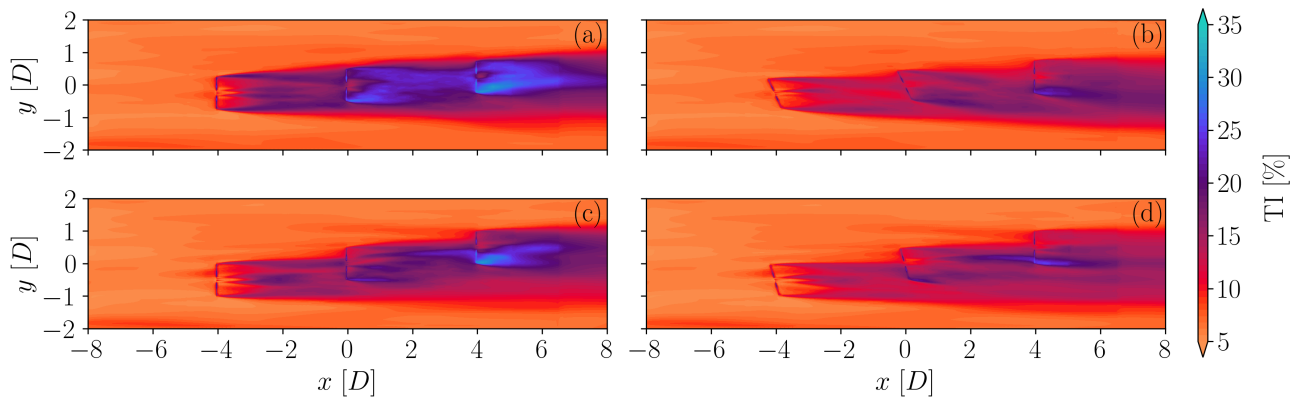


**Figure 11.** Turbulence intensity fields for a TSO power request of  $b = 0.8$ , for two APC control strategies: open loop (OL) (a,c), closed loop with optimal power reserve (CL+MR) (b,d).  $\psi = 3.6^\circ$  (a,b),  $\psi = 7.1^\circ$  (c,d). The slices are extracted at hub height.

Both figures show that at  $b = 0.7$  all methods track power somewhat accurately. In fact, in this case, the power demanded by the TSO is always smaller than the greedy power, and in general, all turbines have enough margin to avoid saturations. As the power demand increases, it gets closer to the available one, leading to inaccuracies in the tracking performance driven by local saturation events. Still, for  $b = 0.8$ , the effectiveness of the closed-loop methods is evident. This is mostly due to the setpoint redistribution logic that makes unsaturated turbines compensate for the tracking error of the saturated ones. However, when  $b > 0.8$ , the power available to the wind farm is often below the maximum available one, and this is especially clear in the time interval  $650 \text{ s} < t < 1000 \text{ s}$ . In such cases, the higher power availability made possible by wake steering allows only CL+MR to track the signal, while other methods clearly lack the margin to do so.

In the zoomed regions of the plots, the saturation events can be clearly observed. In the open-loop case, the power demand remains unaffected since no countermeasure is implemented. Conversely, in the closed-loop cases, it remains constant for saturated rotors since the other rotors are called to compensate.

### 3.4.1 Saturation events

Figures 14 and 15 provide a visual representation of the occurrences of local saturation conditions for each APC strategy and different TSO request scenarios for  $\psi = 3.6^\circ$  and  $\psi = 7.1^\circ$ .

These plots indicate that waked wind turbines – i.e.,  $WT_2$  and  $WT_3$  – are often saturated because of their generally small power reserve. This effect is exacerbated in the scenario with stronger wake impingement when  $\psi = 3.6^\circ$ . CL does not reduce the extent of saturation events compared to OL, but it rather increases them since other turbines are requested to compensate. This results in better APC tracking, as will be shown in Sect. 3.4.2.

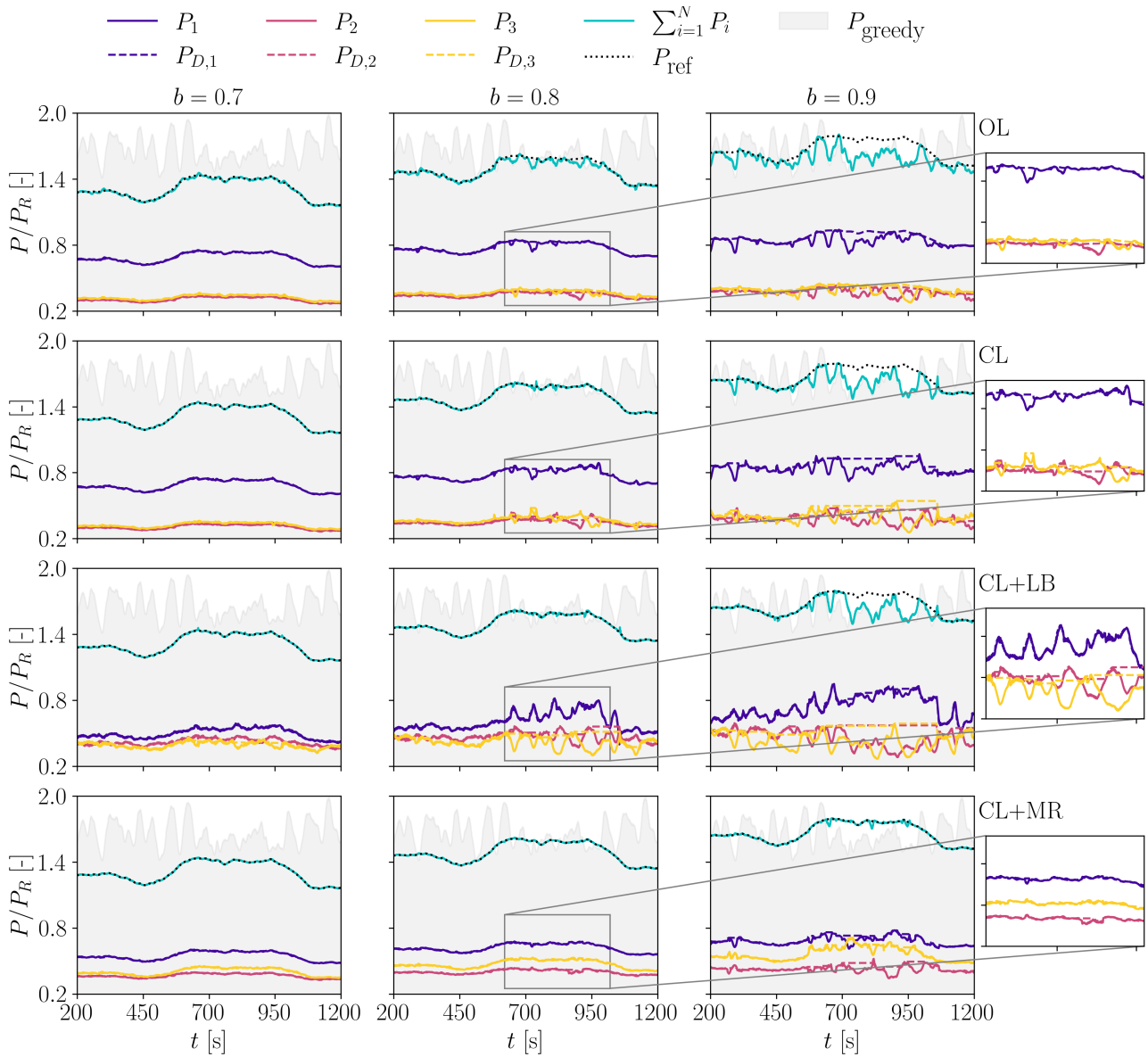


**Figure 12.** Time series of power demand  $P_{D,i}$  and power generated  $P_i$  for  $\psi = 3.6^\circ$ . The  $y$  axes are non-dimensionalized by the rated power  $P_R$  of the IEA 3.4 MW reference wind turbine. The wind farm power obtained in greedy operation (without wake steering) is displayed in the background in grey.

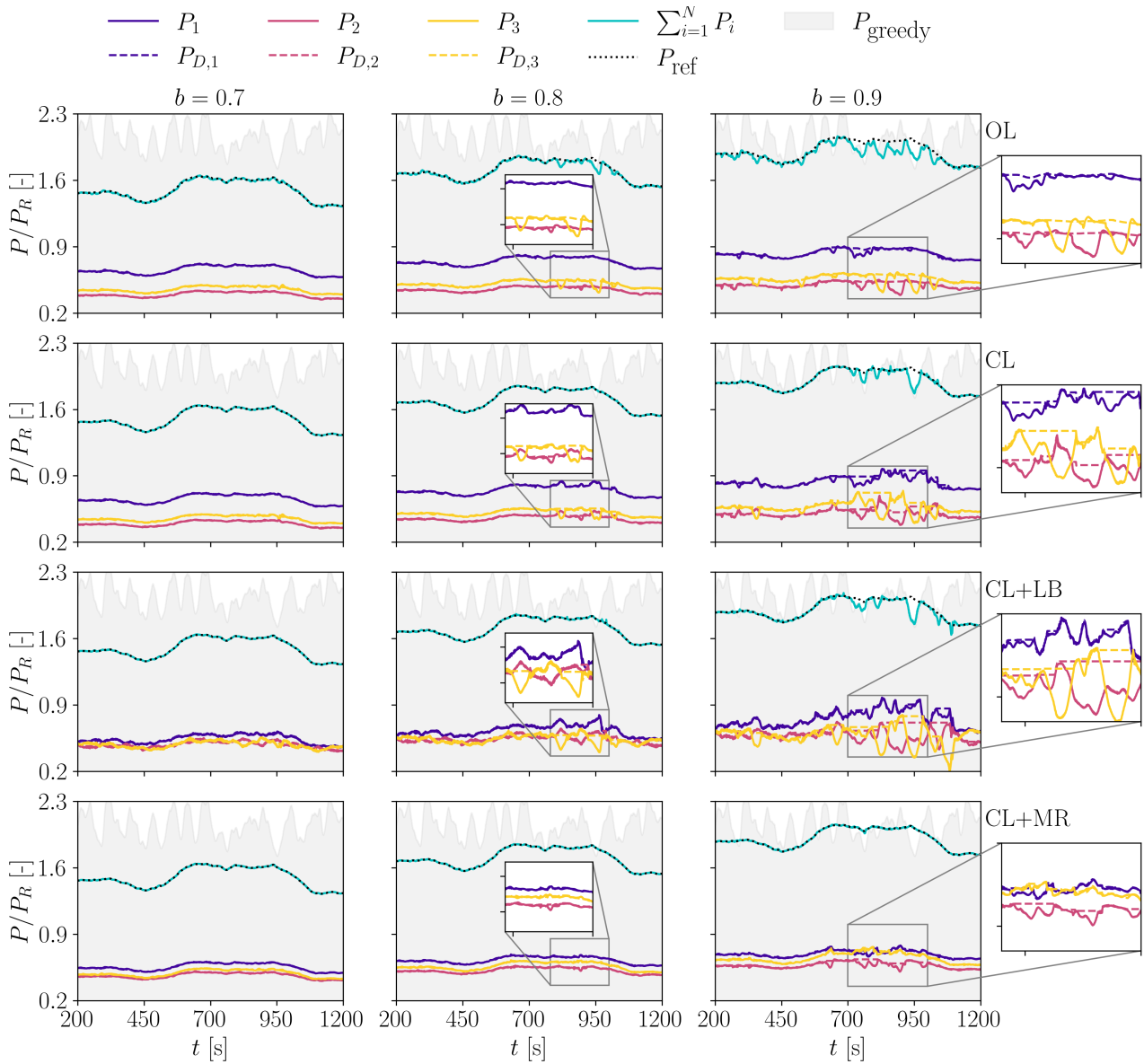


**Figure 13.** Time series of power demand  $P_{D,i}$  and power generated  $P_i$  for  $\psi = 7.1^\circ$ . The  $y$  axes are non-dimensionalized by the rated power  $P_R$  of the IEA 3.4 MW reference wind turbine. The wind farm power obtained in greedy operation (without wake steering) is displayed in the background in grey.

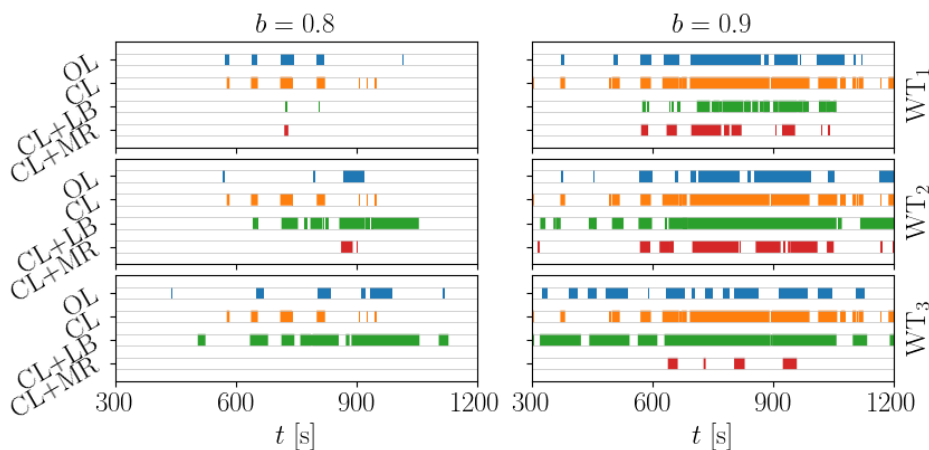


**Figure 14.** Occurrence of local saturation events for the three turbines in the array and the different control strategies for  $\psi = 3.6^\circ$ . Only TSO requests with  $b \geq 0.8$  are considered, as few saturations were observed for  $b = 0.7$ .

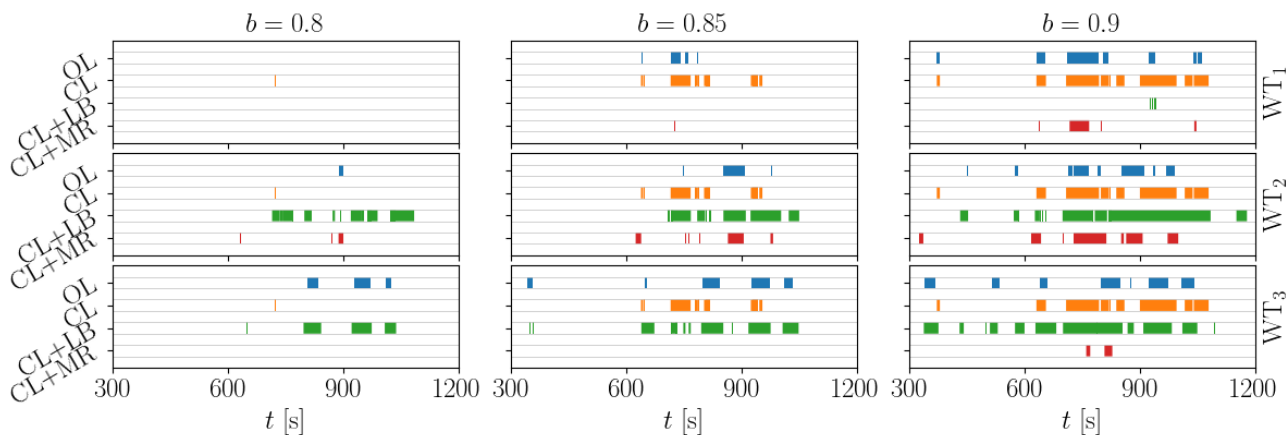


**Figure 15.** Occurrence of local saturation events for the three turbines in the array and the different control strategies for  $\psi = 7.1^\circ$ . Only TSO requests with  $b \geq 0.8$  are considered, as few saturations were observed for  $b = 0.7$ .

The strategy CL+LB presents the highest number of saturation events of waked turbines, while the most upstream turbine is less prone to saturation. This is because, in order to balance the tower base fore-aft bending moment, waked turbines are requested to yield a power that is not actually available. At high power demands (i.e.,  $b > 0.8$ ), waked wind turbines operate in greedy mode, while  $WT_1$  is responsible for following the TSO signal. In this case, the difference between 50% and 75% rotor overlap is remarkable, since in the latter case  $WT_1$  is often saturated, while in the former it is not. This is due to the different wake impingement that modifies the load distribution.

To further understand the reasons for the observed saturation events, the collective blade pitch angle of the turbines  $\theta$  is considered. In fact, this parameter can be seen as a proxy of the local power reserve, as discussed in Sect. 2.4. Figures 16 and 17 show the mean collective blade pitch angle  $\bar{\theta}$ , binned according to the instantaneous amount of power required, normalized by the wind farm available power, as determined from a greedy simulation in the same conditions. This type of binning is chosen to decouple the aerodynamic effects of the APC strategy from sporadic events introduced by the properties of the inflow seed. All simulations with different  $b$  levels are included in the average for a given  $\psi$ , and only bins with a minimum total length of 30 seconds are included. Figure 16 refers to the scenario  $\psi = 3.6^\circ$ , while Fig. 17 refers to results for  $\psi = 7.1^\circ$ .

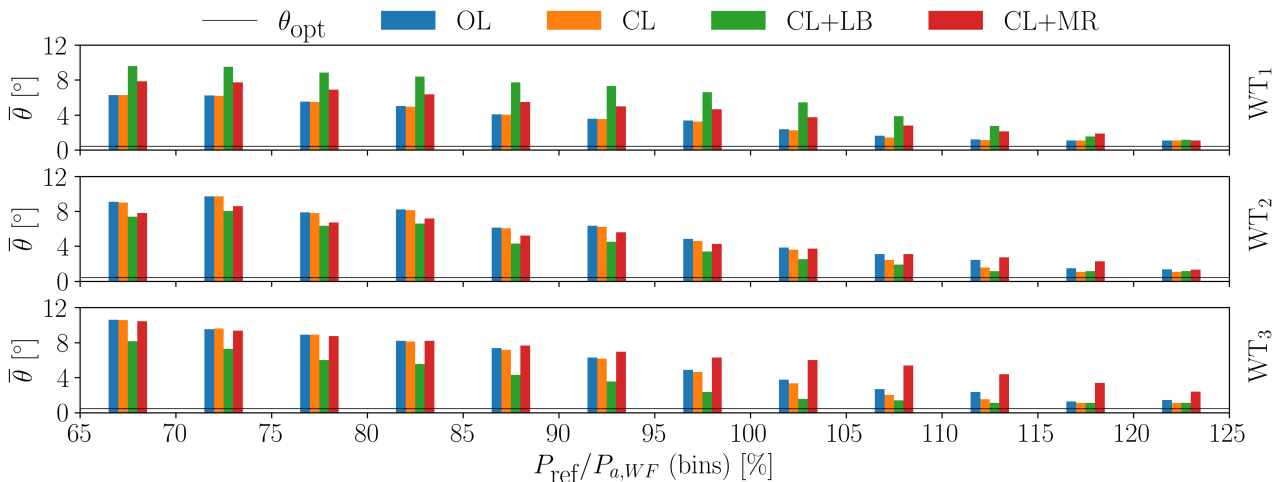


**Figure 16.** Mean collective blade pitch angle binned by the instantaneous available power computed from the time series of greedy power and TSO power request for  $\psi = 3.6^\circ$ . Mean value over the four runs with  $b = b_i$ . Only bins with a minimum total length equivalent to 30 seconds are considered.

These results show that OL and CL share the same power reserve distribution since, in both cases, the same power setpoints  $\alpha_i$  are used. As expected, when the power demand increases, the turbines that operate with CL present a lower  $\bar{\theta}$  than those with OL because of the closed-loop correction and of the setpoint redistribution that occurs with saturations. Consistently with the results shown previously, CL+LB presents a distribution of power reserves that is strongly unbalanced towards the upstream turbine. In fact, the goal of balancing loads implies that waked turbines receive relatively high power demand setpoints, which push them closer to saturation as the power demand increases. The proximity to saturation is visible in Figs. 16 and 17, as the

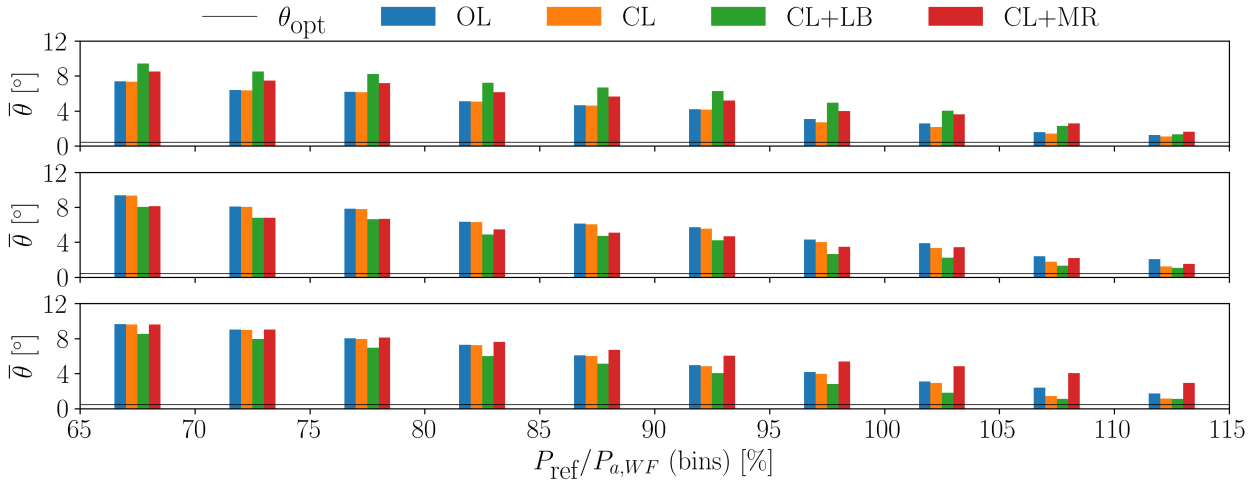


**Figure 17.** Mean collective blade pitch angle binned by the instantaneous available power computed from the time series of greedy power and TSO power request for  $\psi = 7.1^\circ$ . Mean value over the four runs with  $b = b_i$ . Only bins with a minimum total length equivalent to 30 seconds are considered.

error bars approach the optimum pitch angle value  $\theta_{opt}$ . Conversely, the proposed CL+MR approach presents a distribution of reserve that is balanced within the wind farm, resulting in a generally higher power reserve for waked turbines and a lower one for the upstream turbine.

CL+LB appears to be sensitive to the wind direction  $\psi$ , as a strong wake impingement at  $\psi = 3.6^\circ$  yields a more unbalanced power reserve distribution than for  $\psi = 7.1^\circ$ . In the other cases, the effect of  $\psi$  is less evident. This is expected since, in this case, the setpoints depend on the wind direction.

### 3.4.2 Power tracking accuracy

Figure 18 presents the RMS of the power tracking error  $\Delta_P$  for both wind direction (i.e., wake overlap) scenarios.

Results indicate that closed-loop methods can significantly reduce the tracking error compared to the open-loop approach. The effectiveness is higher for  $b \leq 0.8$  and gradually reduces as the power demand is increased, as it appears already in the time series in Figs. 12 and 13. In all cases, the proposed maximum reserve method CL+MR presents the lowest power tracking error. This is to be expected since, for  $b > 0.7$ , there are short events where the power demand exceeds the available greedy power that degrade the tracking accuracy for methods that do not include wake steering.

To perform a more comprehensive comparison, the same analysis is repeated. This time, however, the tracking error time series are binned according to the instantaneous required power normalized by the wind farm available power, as done earlier for  $\bar{\theta}$ . Only bins with a minimum length of 30 seconds are considered, and the values of  $\Delta_P$  in each bin from each power

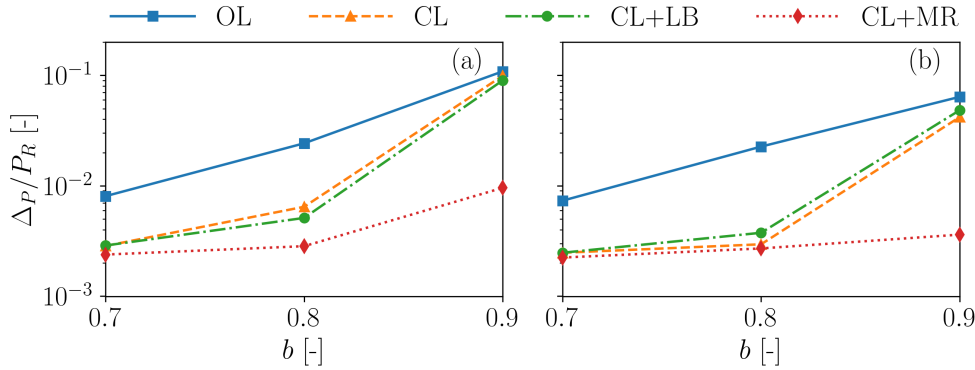


**Figure 18.** RMS of tracking error normalized by the turbine rated power for  $\psi = 3.6^\circ$  (a) and  $\psi = 7.1^\circ$  (b).

365 demand scenario ( $b$  request) are averaged. Only positive values of  $\Delta P$  are considered here, since they represent a lack of power reserve. Results are shown in Figs. 19 and 20 for  $\psi = 3.6^\circ$  and  $\psi = 7.1^\circ$ , respectively.

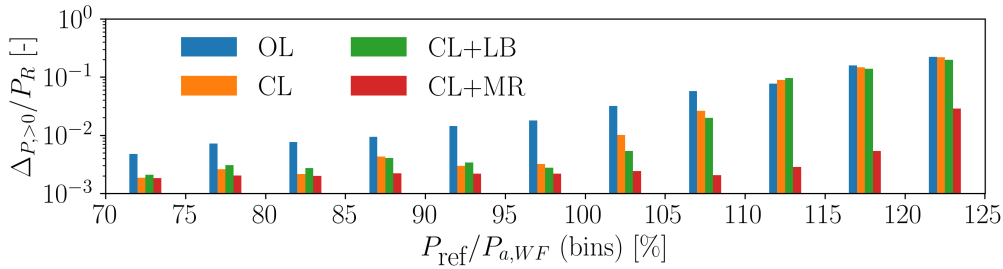


**Figure 19.** Positive tracking error binned by the instantaneous available power computed from the time series of greedy power and TSO power request for  $\psi = 3.6^\circ$ . All values are normalized by the wind turbine rated power. Data from the four runs with different power requests  $b$  are averaged. Only bins with a minimum total length equivalent to 30 seconds are considered.

370 Results indicate that all closed-loop methods perform similarly at moderate TSO demands, i.e.  $b < 0.8$ , with a remarkable performance improvement over OL. The improvement of closed-loop methods is due to the faster response of the wind farm and to the treatment of saturation conditions. As the power demand approaches  $TSO/P_{a,W_F} \approx 100\%$ , the proposed CL+MR improves the tracking accuracy. If, on the one hand, this is to be expected when  $TSO/P_{a,W_F} > 100\%$  due to the overall higher wind farm power, the improvements observed for  $80\% < TSO/P_{a,W_F} < 100\%$  are less obvious. In fact, since CL, CL+LB, and CL+MR share the exact same closed-loop part of the APC controller, the better performance of the new CL+MR is to be attributed to the more balanced power margin distribution, consistently with the mean blade pitch angles shown in Figs. 16 and 17. This is also in agreement with the results of the steady-state analysis shown in Sect. 3.3.

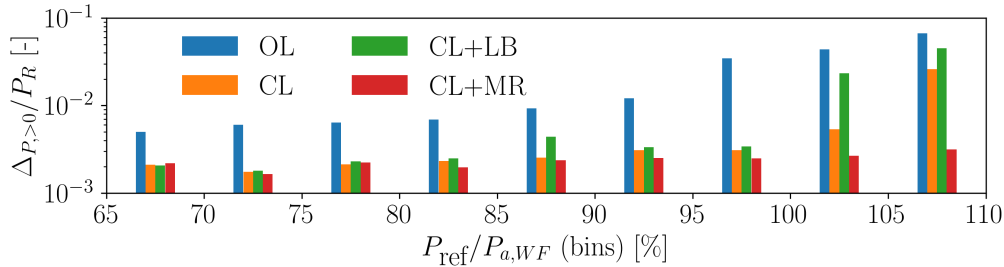


**Figure 20.** Positive tracking error binned by the instantaneous available power computed from the time series of greedy power and TSO power request for  $\psi = 7.1^\circ$ . All values are normalized by the wind turbine rated power. Data from the four runs with different power requests  $b$  are averaged. Only bins with a minimum total length equivalent to 30 seconds are considered.

### 3.4.3 Fatigue analysis

375 Finally, damage equivalent loads (DELs) are computed using the tower base fore-aft bending moment, properly projected to consider the moment orthogonal to the rotor orientation. It is important to mention that simulations were performed with rigid wind turbine models, hence some dynamic effects are neglected. Nevertheless, trends related to each APC strategy should be captured because the type of supercontroller strongly affects the wind turbine aerodynamics and the resulting loads.

Figures 21 and 22 present the DELs of the three wind turbines in the array for  $\psi = 3.6^\circ$  and  $\psi = 7.1^\circ$ , respectively.

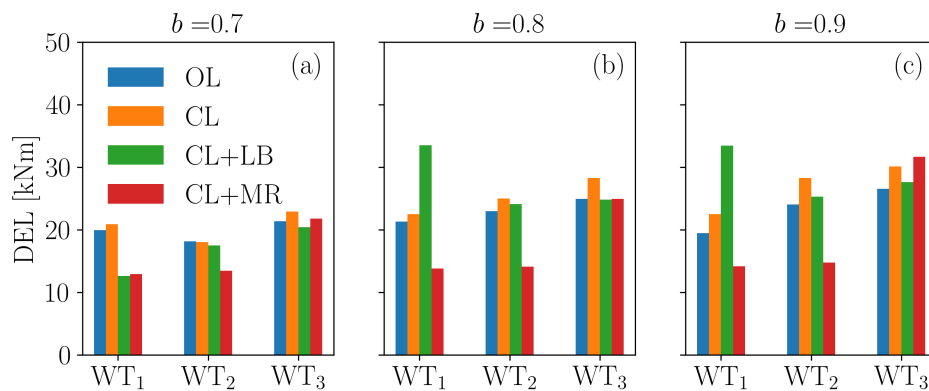


**Figure 21.** DELs of the tower-base fore-aft bending moment for the cases  $b = 0.7$  (a),  $b = 0.8$  (b),  $b = 0.9$  (c), for  $\psi = 3.6^\circ$ .

380 DELs increase along with the parameter  $b$ , due to the associated higher loading. For  $b = 0.7$ ,  $WT_1$  and  $WT_2$  present similar fatigue for OL, CL and CL+MR. In all other cases, the DELs grow as the turbines are impinged by the wakes. In fact,  $WT_3$  is very often the most loaded one, possibly because of the relatively high turbulence associated with partial wake impingements. This is not true in the case of CL+LB, where  $WT_1$  is highly loaded for  $b > 0.7$ . This is explained by the previous analyses (i.e.,

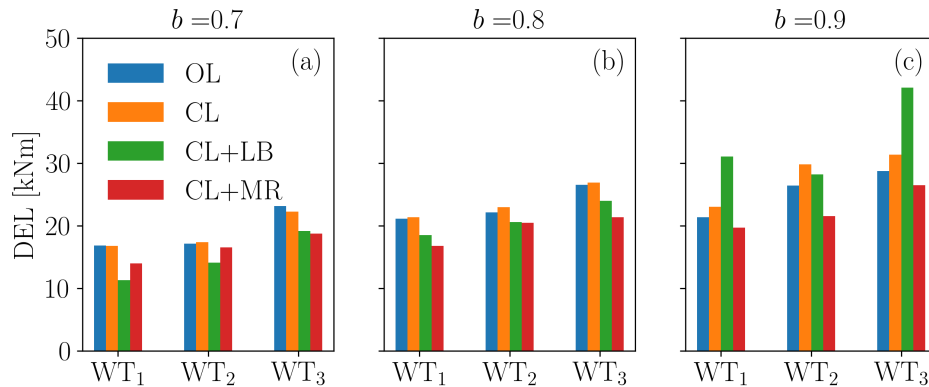


**Figure 22.** DELs of the tower-base fore-aft bending moment for the cases  $b = 0.7$  (a),  $b = 0.8$  (b),  $b = 0.9$  (c), for  $\psi = 7.1^\circ$ .

Fig. 14), which showed that under these circumstances, WT<sub>1</sub> is often the only turbine responsible for tracking the TSO signal, while the waked WT<sub>2</sub> and WT<sub>3</sub> operate in greedy mode.

It is clear that the DELs in Figs. 21 and 22 could be biased by some unique events. These conditions can arise due to the high amplitude cycles that occur especially in correspondence of simultaneous saturation events. For this reason, no further conclusions are drawn; rather, the fatigue analysis is repeated by binning the load time series according to the instantaneously required power, normalized by the wind farm available power, as done already in Sect. 3.4.1. In this case, multiple DELs are computed on continuous time segments of at least 45 seconds that belong to a seed, and they are later summed together. The DELs are computed in this way for each  $b_i$  scenario, and they are then averaged. The results are shown in Figs. 23 and 24 for  $\psi = 3.6^\circ$  and  $\psi = 7.1^\circ$ , respectively. In these plots, all data from every  $b_i$  run are averaged.

These results allow for some further insight into the behavior of the controllers. OL and CL do not present significant differences, as the power share distribution is similar. In these cases, the turbines operating in waked conditions are clearly more damaged than the upstream one. CL+LB works especially well for the simpler case of strong curtailments  $T_{SO}/P_{a,WF} < 80\%$ , with rather low DELs in accordance with Vali et al. (2019). The damage is also well distributed among the wind turbines. Finally, the proposed CL+MR presents a relatively constant damage distribution, with improved performance especially in the more difficult cases for  $T_{SO}/P_{a,WF} > 80\%$ . Results also indicate a strong damage reduction on WT<sub>1</sub> and WT<sub>2</sub> for the larger rotor overlap condition (75%,  $\psi = 3.6^\circ$ ).

#### 400 4 Conclusions and outlook

We have presented a new wind farm APC method to robustly track a reference power signal in turbulent wind conditions. The controller collectively operates the wind turbines with the goal of maximizing the minimum local available power. This reserve can then be exploited for accurate power tracking, ensuring minimal insurgence of saturation events.

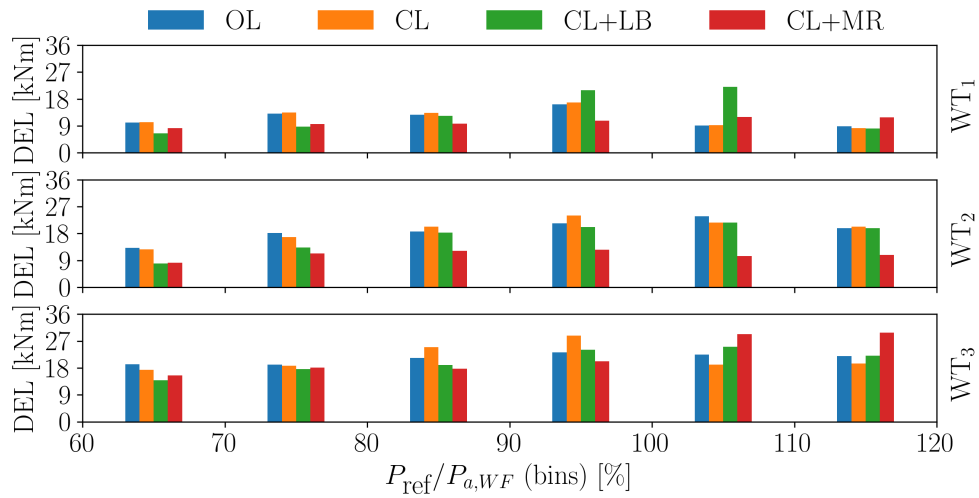


**Figure 23.** DELs of the tower-base fore-aft bending moment for  $\psi = 3.6^\circ$ . The DELs are binned with the instantaneous available power computed with the time series of greedy power and TSO power request. Data from the four runs with  $b = b_i$  are averaged. Only continuous time segments with a minimum duration of 45 seconds are considered.

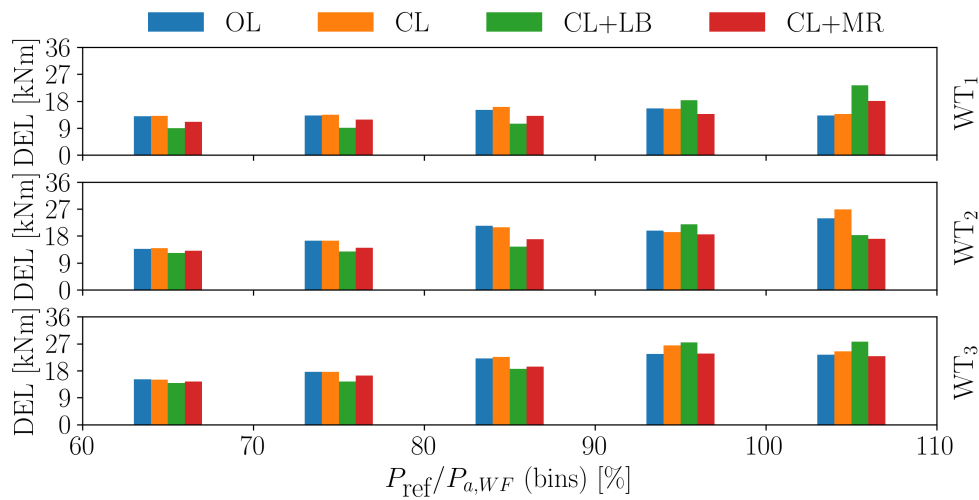


**Figure 24.** DELs of the tower-base fore-aft bending moment for  $\psi = 7.1^\circ$ . The DELs are binned with the instantaneous available power computed with the time series of greedy power and TSO power request. Data from the four runs with  $b = b_i$  are averaged. Only continuous time segments with a minimum duration of 45 seconds are considered.



The algorithm combines one open loop and one closed loop, which operate at different time rates. A modified version of  
405 FLORIS was utilized to compute the wind turbine set points for the open-loop branch in a gradient-based optimization. The PI  
gains of the closed-loop branch were tuned with a digital twin that mimics the wind turbine dynamics, and the propagation of  
wake effects.

The new methodology was tested on a small cluster of three wind turbines with persistent waking. We quantified the power  
reserve with a steady-state analysis and compared the new algorithm with a standard open-loop APC method. We observed that  
410 the new methodology is particularly effective at increasing power reserves when it can mitigate strong wake impingements.

In addition, the new methodology was tested with unsteady LES-ALM simulations, showing an accurate power tracking  
performance, which was, in most cases, largely superior to the one provided by reference controllers representing the state  
of the art in APC. We have shown that this better accuracy is explained by the strong reduction of saturation events and the  
evenly spread power reserve, as measured by the mean collective blade pitch angle. We have binned the data according to the  
415 instantaneous available wind farm power to exclude biasing by isolated events.

Overall, the following observations should be highlighted:

- The power margin of the wind turbines in a wind farm is significantly affected by the entity of wake impingement.
- The new methodology is very effective at creating additional margins when the wind farm operates close to its maximum  
420 power capacity, because wake deficits are particularly strong in those conditions, and the effectiveness of wake steering  
is maximum.
- Power tracking accuracy dramatically depends on the occurrence of saturation events. In this regard, it should be noted  
that:
  - When one wind turbine saturates, it is extremely beneficial to redistribute its power tracking error in the form of  
additional power demand to other turbines that are not saturated.
  - 425 – The main hindrance to tracking accuracy is represented by conditions in which simultaneous saturations occur.  
These can trigger cascading effects of power redistribution, or – in a worst case scenario – can push all wind  
turbines to operate in greedy mode even if the wind farm power demand is exceeded.
  - When applying PI methods, it is extremely important to implement anti-windup procedures to hedge against satu-  
rations.

430 The main limitation of this work is the rather small duration of the LES-ALM simulations. Although in line with similar  
studies in the literature, this limited duration could have biased some results due to particular events occurring within the inflow  
time histories. To account for this, we performed greedy simulations to quantify the actual wind farm available power at every  
time instant. Another limitation of the unsteady results is the use of rigid wind turbine models in the simulations. If, on the one  
hand, this is not expected to play a major role in the behavior of wakes, on the other it somehow limits the conclusions that can  
435 be drawn on the analysis of fatigue.



## Appendix A: Nomenclature

<b>A</b>	Ambient conditions
$b$	Shift of normalized power demand signal
$C_P$	Power coefficient
440 $C_T$	Thrust coefficient
$c$	Amplitude of normalized power demand signal
$D$	Rotor diameter
$K^I$	Control gain (integral)
$K^P$	Control gain (proportional)
445 $m$	Power reserve
$n_k^{AGC}$	Normalized power demand perturbation
$P$	Wind turbine power
$P_D$	Wind turbine power demand
$P_R$	Rated power
450 $P_{ref}$	Reference power signal
$R$	Rotor radius
$s$	Saturation
$t$	Time
$U$	Rotor-equivalent wind speed
455 $U_\infty$	Free-stream wind speed at hub height
<b>u</b>	Control inputs
$x$	Cartesian coordinate
$y$	Cartesian coordinate
$z$	Cartesian coordinate
460	
$\alpha$	Power-share setpoint
$\Delta_L$	Load balancing error
$\Delta_P$	Power tracking error
$\epsilon$	Curtailment
465 $\eta_P$	Power loss factor
$\gamma$	Rotor yaw angle
$\lambda$	Tip speed ratio
$\Omega$	Rotor angular speed
$\Omega_R$	Rated rotor angular speed



470	$\psi$	Wind direction
	$\rho$	Air density
	$\theta$	Blade pitch angle
	AGC	Automatic Generation Control
475	APC	Active Power Control
	CL	Closed loop
	CLD	Coordinated load distribution
	CL+LB	Closed loop with load-balancing
	CL+MR	Closed loop with maximum reserve
480	DEL	Damage Equivalent Load
	FA	Fore-Aft
	FLORIS	FLOW Redirection and Induction in Steady State
	OL	Open loop
	PI	Proportional – integral
485	RMS	Root Mean Square
	SOWFA	Simulator fOR Wind Farm Applications
	TI	Turbulence Intensity
	TSO	Transmission System Operator
	WF	Wind Farm
490	WT	Wind Turbine

*Code and data availability.* The supercontroller codes in C++ are available on Zenodo at <https://doi.org/10.5281/zenodo.14716525>. Videos of one of the simulations are available at [https://youtu.be/dS\\_FrPhw3EM](https://youtu.be/dS_FrPhw3EM).

*Author contributions.* CLB developed the formulation of the new APC method and supervised the overall research. ST implemented the model, performed the experiments, and conducted the steady-state analyses with FLORIS. FC supported the implementation of the methods. All authors contributed to the interpretation of the results. CLB and ST wrote the manuscript, with contributions by FC. All authors provided important input to this research work through discussions and feedback and improved the manuscript.

*Competing interests.* The authors declare that they have no conflict of interest, except for CLB, who is the Editor in Chief of the Wind Energy Science journal.



500 *Financial support.* This work has been supported in part by the PowerTracker project, which receives funding from the German Federal Ministry for Economic Affairs and Climate Action (FKZ: 03EE2036A). This work has also been partially supported by the MERIDIONAL, SUDOCO and TWAIN projects, which receive funding from the European Union’s Horizon Europe Programme under grant agreements 101084216, 101122256, and 101122194 respectively.

505 *Acknowledgements.* The authors express their gratitude to the Leibniz Supercomputing Centre (LRZ) for providing access and computing time on the SuperMUC Petascale System under Projekt-ID pr84be “Large-Eddy Simulation for Wind Farm Control”. The authors would like to thank Abhinav Anand for the support in the implementation of the steady-state model.



## References

- Aho, J., Buckspan, A., Laks, J., Fleming, P., Jeong, Y., Dunne, F., Churchfield, M., Pao, L., and Johnson, K.: A tutorial of wind turbine control for supporting grid frequency through active power control, in: 2012 American Control Conference (ACC), pp. 3120–3131, 510 <https://doi.org/10.1109/ACC.2012.6315180>, 2012.
- Bertelè, M., Bottasso, C. L., and Schreiber, J.: Wind inflow observation from load harmonics: initial steps towards a field validation, *Wind Energy Science*, 6, 759–775, <https://doi.org/10.5194/wes-6-759-2021>, 2021.
- Bertelè, M., Meyer, P. J., Sucameli, C. R., Fricke, J., Wegner, A., Gottschall, J., and Bottasso, C. L.: The rotor as a sensor – Observing shear and veer from the operational data of a large wind turbine, *Wind Energy Science*, 9, 1419—1429, [https://doi.org/10.5194/wes-9-1419-](https://doi.org/10.5194/wes-9-1419-2024) 515 2024, 2024.
- Boersma, S., Rostampour, V., Doekemeijer, B., van Geest, W., and van Wingerden, J.-W.: A constrained model predictive wind farm controller providing active power control: an LES study, *Journal of Physics: Conference Series*, 1037, 032 023, <https://doi.org/10.1088/1742-6596/1037/3/032023>, 2018.
- Bortolotti, P., Tarres, H. C., Dykes, K. L., Merz, K., Sethuraman, L., Verelst, D., and Zahle, F.: IEA Wind TCP Task 37: Systems Engineering in Wind Energy - WP2.1 Reference Wind Turbines, Tech. rep., National Renewable Energy Lab. (NREL), 520 <https://doi.org/10.2172/1529216>, 2019.
- Bossanyi, E. A.: The Design of closed loop controllers for wind turbines, *Wind Energy*, 3, 149–163, <https://doi.org/https://doi.org/10.1002/we.34>, 2000.
- Brayton, R., Director, S., Hachtel, G., and Vidigal, L.: A new algorithm for statistical circuit design based on quasi-Newton methods and function splitting, *IEEE Transactions on Circuits and Systems*, 26, 784–794, <https://doi.org/10.1109/TCS.1979.1084701>, 1979. 525
- Campagnolo, F., Petrović, V., Schreiber, J., Nanos, E. M., Croce, A., and Bottasso, C. L.: Wind tunnel testing of a closed-loop wake deflection controller for wind farm power maximization, *Journal of Physics: Conference Series*, 753, 032 006, <https://doi.org/10.1088/1742-6596/753/3/032006>, 2016.
- Campagnolo, F., Castellani, F., Natili, F., Astolfi, D., and Mühle, F.: Wind Tunnel Testing of Yaw by Individual Pitch Control Applied to Wake Steering, *Frontiers in Energy Research*, 10, <https://doi.org/10.3389/fenrg.2022.883889>, 2022. 530
- Campagnolo, F., Tamaro, S., Mühle, F., and Bottasso, C. L.: Wind Tunnel Testing of Combined Derating and Wake Steering, *IFAC-PapersOnLine*, 56, 8400–8405, <https://doi.org/https://doi.org/10.1016/j.ifacol.2023.10.1034>, 22nd IFAC World Congress, 2023.
- Cossu, C.: Wake redirection at higher axial induction, *Wind Energy Science*, 6, 377–388, <https://doi.org/10.5194/wes-6-377-2021>, 2021.
- Doekemeijer, B. M., Kern, S., Maturu, S., Kanev, S., Salbert, B., Schreiber, J., Campagnolo, F., Bottasso, C. L., Schuler, S., Wilts, F., Neumann, T., Potenza, G., Calabretta, F., Fioretti, F., and van Wingerden, J.-W.: Field experiment for open-loop yaw-based wake steering at a commercial onshore wind farm in Italy, *Wind Energy Science*, 6, 159–176, <https://doi.org/10.5194/wes-6-159-2021>, 2021. 535
- Ela, E., Gevorgian, V., Fleming, P., Zhang, Y. C., Singh, M., Muljadi, E., Scholbrook, A., Aho, J., Buckspan, A., Pao, L., Singhvi, V., Tuohy, A., Pourbeik, P., Brooks, D., and Bhatt, N.: Active Power Controls from Wind Power: Bridging the Gaps, Tech. Rep. NREL/TP-5D00-60574, National Renewable Energy Lab. (NREL), <https://doi.org/10.2172/1117060>, 2014.
- Fleming, P., Aho, J., Gebraad, P., Pao, L., and Zhang, Y.: Computational fluid dynamics simulation study of active power control in wind plants, in: 2016 American Control Conference (ACC), pp. 1413–1420, <https://doi.org/10.1109/ACC.2016.7525115>, 2016. 540
- Fleming, P., King, J., Dykes, K., Simley, E., Roadman, J., Scholbrook, A., Murphy, P., Lundquist, J. K., Moriarty, P., Fleming, K., van Dam, J., Bay, C., Mudafort, R., Lopez, H., Skopek, J., Scott, M., Ryan, B., Guernsey, C., and Brake, D.: Initial results from a field campaign



- of wake steering applied at a commercial wind farm – Part 1, *Wind Energy Science*, 4, 273–285, <https://doi.org/10.5194/wes-4-273-2019>, 2019.
- 545 Fleming, P. A., Gebraad, P. M., Lee, S., van Wingerden, J.-W., Johnson, K., Churchfield, M., Michalakes, J., Spalart, P., and Moriarty, P.: Evaluating techniques for redirecting turbine wakes using SOWFA, *Renewable Energy*, 70, 211–218, <https://doi.org/https://doi.org/10.1016/j.renene.2014.02.015>, special issue on aerodynamics of offshore wind energy systems and wakes, 2014.
- 550 Gebraad, P. M. O., Teeuwisse, F. W., van Wingerden, J. W., Fleming, P. A., Ruben, S. D., Marden, J. R., and Pao, L. Y.: Wind plant power optimization through yaw control using a parametric model for wake effects—a CFD simulation study, *Wind Energy*, 19, 95–114, <https://doi.org/https://doi.org/10.1002/we.1822>, 2016.
- Guilloré, A., Campagnolo, F., and Bottasso, C. L.: A control-oriented load surrogate model based on sector-averaged inflow quantities: capturing damage for unwaked, waked, wake-steering and curtailed wind turbines, *Journal of Physics: Conference Series*, 2767, 032019, <https://doi.org/10.1088/1742-6596/2767/3/032019>, 2024.
- 555 Heck, K., Johlas, H., and Howland, M.: Modelling the induction, thrust and power of a yaw-misaligned actuator disk, *Journal of Fluid Mechanics*, 959, A9, <https://doi.org/10.1017/jfm.2023.129>, 2023.
- Jensen, N.: A note on wind generator interaction, no. 2411 in *Risø-M, Risø National Laboratory*, ISBN 87-550-0971-9, 1983.
- Jiménez, A., Crespo, A., and Migoya, E.: Application of a LES technique to characterize the wake deflection of a wind turbine in yaw, *Wind Energy*, 13, 559–572, <https://doi.org/https://doi.org/10.1002/we.380>, 2010.
- 560 Kanev, S., Savenije, F., and Engels, W.: Active wake control: An approach to optimize the lifetime operation of wind farms, *Wind Energy*, 21, 488–501, <https://doi.org/https://doi.org/10.1002/we.2173>, 2018.
- King, J., Fleming, P., King, R., Martínez-Tossas, L. A., Bay, C. J., Mudafort, R., and Simley, E.: Control-oriented model for secondary effects of wake steering, *Wind Energy Science*, 6, 701–714, <https://doi.org/10.5194/wes-6-701-2021>, 2021.
- 565 Lee, S., Churchfield, M. J., Moriarty, P. J., Jonkman, J., and Michalakes, J.: A Numerical Study of Atmospheric and Wake Turbulence Impacts on Wind Turbine Fatigue Loadings, *Journal of Solar Energy Engineering*, 135, <https://doi.org/10.1115/1.4023319>, 031001, 2013.
- Liew, J. and Larsen, G. C.: How does the quantity, resolution, and scaling of turbulence boxes affect aeroelastic simulation convergence?, *Journal of Physics: Conference Series*, 2265, 032049, <https://doi.org/10.1088/1742-6596/2265/3/032049>, 2022.
- Liew, J., Urbán, A. M., and Andersen, S. J.: Analytical model for the power–yaw sensitivity of wind turbines operating in full wake, *Wind Energy Science*, 5, 427–437, <https://doi.org/10.5194/wes-5-427-2020>, 2020.
- 570 Medici, D. and Alfredsson, P. H.: Measurements on a wind turbine wake: 3D effects and bluff body vortex shedding, *Wind Energy*, 9, 219–236, <https://doi.org/https://doi.org/10.1002/we.156>, 2006.
- Meyer Forsting, A. R., Pirrung, G. R., and Ramos-García, N.: A vortex-based tip/smearing correction for the actuator line, *Wind Energy Science*, 4, 369–383, <https://doi.org/10.5194/wes-4-369-2019>, 2019.
- 575 Meyers, J., Bottasso, C. L., Dykes, K., Fleming, P., Gebraad, P., Giebel, G., Göçmen, T., and van Wingerden, J.-W.: Wind Farm Flow Control: Prospects and Challenges, *Wind Energy Science*, 7, 2271–2306, <https://doi.org/10.5194/wes-7-2271-2022>, 2022.
- National Renewable Energy Laboratory: floris v3, <https://github.com/NREL/floris>, <https://doi.org/10.5281/zenodo.6320841>, 2023.
- Oudich, Y., Gyselinck, J., De Belie, F., and Kinnaert, M.: Providing power reserve for secondary grid frequency regulation of offshore wind farms through yaw control, *Wind Energy*, 26, 850–873, <https://doi.org/https://doi.org/10.1002/we.2845>, 2023.
- 580 Schottler, J., Mühle, F., Bartl, J., Peinke, J., Adaramola, M. S., Sætran, L., and Hölling, M.: Comparative study on the wake deflection behind yawed wind turbine models, *Journal of Physics: Conference Series*, 854, 012032, <https://doi.org/10.1088/1742-6596/854/1/012032>, 2017.



- Shapiro, C. R., Bauweraerts, P., Meyers, J., Meneveau, C., and Gayme, D. F.: Model-based receding horizon control of wind farms for secondary frequency regulation, *Wind Energy*, 20, 1261–1275, <https://doi.org/https://doi.org/10.1002/we.2093>, 2017.
- 585 Silva, J. G., Doekemeijer, B. M., Ferrari, R., and van Wingerden, J.-W.: Active power control of wind farms: an instantaneous approach on waked conditions, *Journal of Physics: Conference Series*, 2265, 022 056, <https://doi.org/10.1088/1742-6596/2265/2/022056>, 2022.
- Sinner, M., Spyrou, E., Bay, C. J., King, J., and Corbus, D.: Coordinated wind power plant and battery control for active power services, *Journal of Renewable and Sustainable Energy*, 15, 053 304, <https://doi.org/10.1063/5.0156464>, 2023.
- Starke, G. M., Meneveau, C., King, J., and Gayme, D. F.: Yaw-Augmented Control for Wind Farm Power Tracking, in: 2023 American Control Conference (ACC), pp. 184–191, <https://doi.org/10.23919/ACC55779.2023.10156444>, 2023.
- 590 Tamaro, S. and Bottasso, C. L.: A New Wind Farm Active Power Control Strategy to Boost Tracking Margins in High-demand Scenarios, in: 2023 American Control Conference (ACC), pp. 192–197, <https://doi.org/10.23919/ACC55779.2023.10156275>, 2023.
- Tamaro, S., Campagnolo, F., and Bottasso, C. L.: On the power and control of a misaligned rotor – beyond the cosine law, *Wind Energy Science*, 9, 1547–1575, <https://doi.org/10.5194/wes-9-1547-2024>, 2024a.
- Tamaro, S., Guilloré, A., Anand, A., Mühle, F. V., Campagnolo, F., and Bottasso, C. L.: Validation of induction/steering reserve-boosting active power control by a wind tunnel experiment with dynamic wind direction changes, *Journal of Physics: Conference Series*, 2767, 092 067, <https://doi.org/10.1088/1742-6596/2767/9/092067>, 2024b.
- 595 The MathWorks Inc.: MATLAB version: 9.13.0 (R2022b), 2022.
- Troldborg, N., Sørensen, J. N., and Mikkelsen, R.: Actuator Line Simulation of Wake of Wind Turbine Operating in Turbulent Inflow, *Journal of Physics: Conference Series*, 75, 012 063, <https://doi.org/10.1088/1742-6596/75/1/012063>, 2007.
- 600 Vali, M., Petrović, V., Steinfeld, G., Y. Pao, L., and Kühn, M.: An active power control approach for wake-induced load alleviation in a fully developed wind farm boundary layer, *Wind Energy Science*, 4, 139–161, <https://doi.org/10.5194/wes-4-139-2019>, 2019.
- van Kuik, G., Peinke, J., Nijssen, R., Lekou, D., Mann, J., Sørensen, J., Ferreira, C., van Wingerden, J., Schlipf, D., Gebraad, P., Polinder, H., Abrahamsen, A., van Bussel, G., Sørensen, J., Tavner, P., Bottasso, C., Muskulus, M., Matha, D., Lindeboom, H., Degraer, S., Kramer, O., Lehnhoff, S., Sonnenschein, M., Sørensen, P., Künneke, R., Morthorst, P., and Skytte, K.: Long-term research challenges in wind energy – a research agenda by the European Academy of Wind Energy, *Wind Energy Science*, 1, 1–39, <https://doi.org/10.5194/wes-1-1-2016>, 2016.
- 605 van Wingerden, J.-W., Pao, L., Aho, J., and Fleming, P.: Active Power Control of Waked Wind Farms, *IFAC-PapersOnLine*, 50, 4484–4491, <https://doi.org/https://doi.org/10.1016/j.ifacol.2017.08.378>, 20th IFAC World Congress, 2017.
- Vermeer, L., Sørensen, J., and Crespo, A.: Wind turbine wake aerodynamics, *Progress in Aerospace Sciences*, 39, 467–510, [https://doi.org/https://doi.org/10.1016/S0376-0421\(03\)00078-2](https://doi.org/https://doi.org/10.1016/S0376-0421(03)00078-2), 2003.
- 610 Vollmer, L., Steinfeld, G., Heinemann, D., and Kühn, M.: Estimating the wake deflection downstream of a wind turbine in different atmospheric stabilities: an LES study, *Wind Energy Science*, 1, 129–141, <https://doi.org/10.5194/wes-1-129-2016>, 2016.
- Wang, C.: Numerical simulation of wind farm control, Ph.D. thesis, Technische Universität München, <https://mediatum.ub.tum.de/1578640>, 2021.
- 615 Wang, J., Wang, C., Campagnolo, F., and Bottasso, C. L.: Wake behavior and control: comparison of LES simulations and wind tunnel measurements, *Wind Energy Science*, 4, 71–88, <https://doi.org/10.5194/wes-4-71-2019>, 2019.